Ocean Modelling 129 (2018) 93–103

Contents lists available at ScienceDirect

Ocean Modelling

journal homepage: www.elsevier.com/locate/ocemod

Langmuir turbulence in horizontal salinity gradient

Yalin Fan[a,*], Ewa Jarosz[a], Zhitao Yu[a], W. Erick Rogers[a], Tommy G. Jensen[a], Jun-Hong Liang[b]

[a] Oceanography Division, U.S. Naval Research Laboratory, Stennis Space Center, MS 39529, United States
[b] Louisiana State University, Baton Rouge, LA, United States

ABSTRACT

Langmuir circulation (LC) is believed to be one of the leading causes of turbulent mixing in the upper ocean. Large eddy simulation (LES) models that solve the Craik–Leibovich equations are used to study LC in the upper ocean, yielding new insights that could not be obtained from field observations or turbulent closure models alone. The present study expands our previous LES modeling investigations of LC to real ocean conditions with large-scale environmental motion due to strong horizontal density gradient, which is introduced to the LES model through scale separation analysis. The model is applied to field observations in the Gulf of Mexico when a measurement site was impacted by fresh water inflow. Model results suggest that LC can enhance turbulence in the water column and deepen the mixed layer (ML) with or without the large scale motions, being consistent with previous studies. The strong salinity gradient is shown to be able to reduce the mean flow in the ML, align Langmuir cells with the pressure gradient direction and inhibit turbulence in the ocean surface boundary layer.

1. Introduction

Langmuir circulation (LC), often represented by windrows on the water surface, which are caused by buoyant materials such as gas bubbles in horizontal counter-rotating cells aligned in the wind direction, is believed to be one of the leading causes of turbulent mixing in the upper ocean (Li et al., 1995; Skylingstad and Denbo, 1995; Kukulka et al., 2009; Kukulka et al., 2010; McWilliams et al., 1997; Hamlington et al., 2014). It is important for momentum and heat exchange across the mixed layer (ML), and can directly impact dynamics and thermodynamics in the upper ocean and the lower atmosphere including the vertical distributions of chemical, biological, optical, and acoustic properties.

The dynamical origin of LC is understood as wind-driven shear instability in combination with Stokes drift. The prevailing theoretical interpretation of Langmuir cells is derived by Craik and Leibovich (1976) who introduced effects of waves on Eulerian mean flow into the Navier–Stokes equations. Based on their theory, large eddy simulation (LES) models have been developed to simulate phase-averaged (over high-frequency surface gravity waves) equations for oceanic currents in the surface boundary layer and their interactions with surface gravity waves (Skylingstad and Denbo, 1995; McWilliams et al., 1997). These equations have additional terms proportional to the Lagrangian Stokes drift of the waves, including vortex and Coriolis forces and tracer advection.

LES models have been used to simulate LC in the upper ocean, yielding new insights that could not be obtained from field observations and turbulent closure models. Due to its high computational cost, LES models are usually limited to a finite domain with hundreds of meters at each horizontal direction and cannot resolve large-scale flows. Furthermore, most LES models used in the LC simulations use periodic boundary conditions in the horizontal directions, which assumes the physical properties (i.e. temperature and salinity) and expected flow patterns in the area of interest are of a periodically repeating nature so that the small LES domain is representative for a larger area. Using periodic boundary conditions can significantly reduce computational effort, and it is a good assumption for isotropic shear turbulence. However, LC is anisotropic (McWilliams et al., 1997) and has been observed to be modulated by crosswind tidal currents (Kukulka et al., 2011; Martinat et al., 2011). Idealized LES studies also indicate that LC could interact with oceanic fronts (Hamlington et al., 2014) and standing internal waves (Chini and Leibovich, 2005; Polton et al., 2008).

The present study expands our previous LES modeling investigations of Langmuir turbulence to real ocean conditions with large-scale environmental motion that features fresh water inflow into the study region. The outline of this paper is as follows. A brief description of the implementation of large-scale temperature and salinity variations in the LES model, the observations in the Gulf of Mexico, and the experiment set up are given in Section 2. Results are analyzed in Section 3, and discussion and concluding remarks are presented in Section 4.

2. Method

2.1. Observations in the Gulf of Mexico

A comprehensive field experiment took placed in the Gulf of Mexico

* Correspondence author.
E-mail addresses: yalin.fan@nrlssc.navy.mil (Y. Fan), ewa.jarosz@nrlssc.navy.mil (E. Jarosz).

https://doi.org/10.1016/j.ocemod.2018.07.010
Received 20 November 2017; Received in revised form 24 July 2018; Accepted 26 July 2018
Available online 27 July 2018
1463-5003/ Published by Elsevier Ltd.

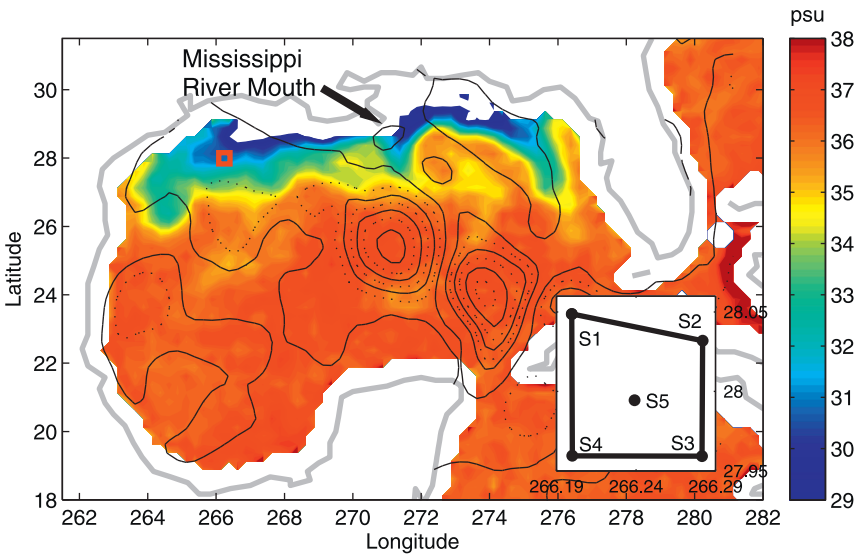

Fig. 1. Composition of 8-days (July 7–14) level 3 map gridded sea surface salinity product (color) derived from NASA "Soil Moisture Active Passive" satellite mission and 7-days (July 13–19) sea surface height anomalies (solid and dotted contour lines in cm) obtained from University of Colorado (UC) Colorado Center for Astrodynamics Research. The red open square represents the location of the field measurements with detailed station locations given in the small insert map. (For interpretation of the references to colour in this figure legend, the reader is referred to the web version of this article.)

from 2 July to 22 July 2016 and was a part of "Turbulence in the Ocean Surface Boundary Layer" project funded by the Naval Research Laboratory. It was conducted on the outer shelf in the Gulf about 190 km southeast of Galveston, TX (Fig. 1). The experiment took place after high discharges from the Mississippi/Atchafalaya River System into the Gulf in the first six months of 2016 with the 2016 mean discharge of 18,531 m^3/s that was higher than the long-term mean discharge value of 16,792 m^3/s. The Mississippi discharge was above the long-term mean between January 1, 2016 and June 15, 2016, and it varied between 18,531 m^3/s and 37,661 m^3/s. It dropped below the 2016 and long-term means just before the experiment began (discharge data are from https://nwis.waterdata.usgs.gov). As show by the NASA sea surface salinity (SSS) in Fig. 1, the fresher water spread along the coast to the east and west of the river mouths, and also slowly pushed southward. The experimental site was located within a strong salinity gradient region (~5 psu per ~100 km).

Temperature, conductivity (salinity), and pressure observations were collected using Sea-Bird Electronics (SBE) 37-SM MicroCAT instruments at the four corners of a nearly square 10 km by 10 km box (S1 to S4). These water properties were measured at 7 levels in the top 11 m, then every ~7 m between 11 m and 50 m, and every 10 m when deeper than 50 m. Additional measurements were collected at the center of the box at station S5. At this location, a Wirewalker (Pinkel et al., 2011) collected detailed temperature (SBE 3) and conductivity (SBE 4) profiles at very fine vertical resolution (< 3 cm) from near the bottom to ~2 m below the sea surface (Fig. 2). A 1200 kHz Teledyne RDI acoustic Doppler current profiler (ADCP) with a wave package deployed at ~ 10 m below the sea surface delivered current velocity profiles (Fig. 7a, b), pressure, and echo intensity. These observations were used to estimate surface wave parameters and spectra (e.g. Terray et al., 1999), which are given in frequency bands range from 0.0083 to 0.9927 Hz with a 0.0156 Hz frequency band width. An example of the wave spectra is given at 14:17 UTC on July 13 in Fig. 3d. It clearly shows that most of the wave energy is concentrated in the frequency bands lower than 0.5 Hz. The 300 kHz bottom-mounted ADCPs were also deployed to measure current profiles at 5 mooring sites (S1 – S5). Meteorology observations such as wind speed and direction (Fig. 3a), air temperature, solar radiation, and relative humidity, were collected by sensors mounted on the research ship (R/V Pelican) that remained inside or just outside the study area during the entire experiment.

2.2. Model description

The LES model used in this study was first introduced by

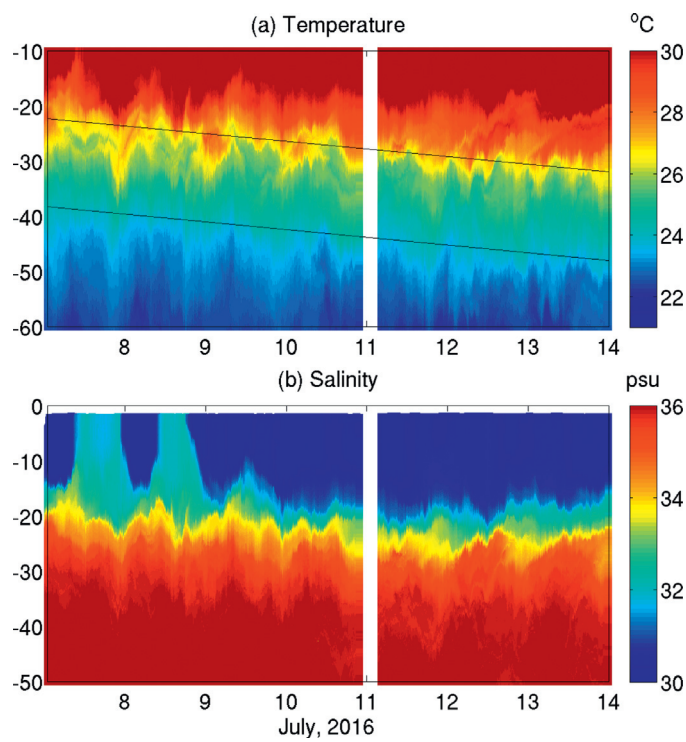

Fig. 2. Vertical profiles of (a) temperature and (b) salinity at S5 from July 7 00:00 UTC to July 14 00:00 UTC. The dashed lines in (a) are added to emphasize the slopping of temperature with time.

McWilliams et al., (1997) to solve the flow components using the wave-phase-averaged Craik–Leibovich theory (e.g., Craik and Leibovich, 1976; Suzuki and Fox–Kemper, 2016) with the effect of wave on current through the vortex force, Stokes–Coriolis force, Lagrangian mean advection associated with Stokes drift, and a wave-averaged increment to pressure that arises through conservative wave–current interactions.

The filtered Craik–Leibovich momentum equation is given as (McWilliams et al., 1997)

$$\frac{D\vec{u}}{Dt} + f\vec{z} \times (\vec{u} + \vec{u}_s) = -\nabla\pi - g\vec{z}\,(\rho/\rho_0) + \vec{u}_s \times \vec{\omega} + SGS, \tag{1}$$

where g is the gravitational acceleration, $D/Dt = \partial_t + \vec{u}\cdot\nabla$, $\vec{u}$ (u, v, w) is the current velocity vector, $\vec{u}_s$ (u_{sx}, u_{sy}) is the Stokes drift vector, and

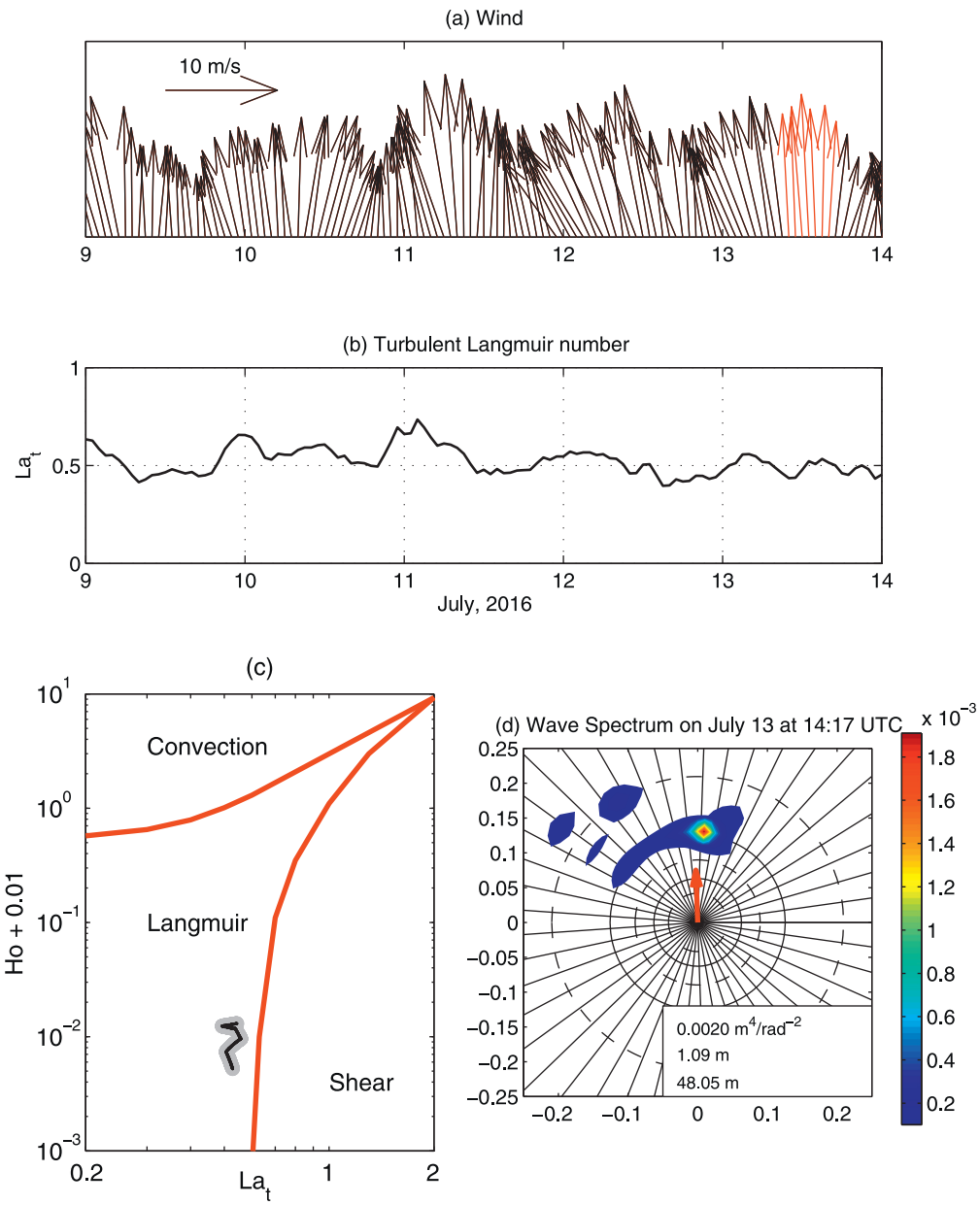

Fig. 3. (a) Wind vectors and (b) turbulent Langmuir number from July 9 00:00 UTC to July 14 00:00 UTC. The red arrows in (a) highlights the period from July 13 10:00 UTC to 15:00 UTC when the winds are roughly unidirectional towards the north with small magnitude variations. (c) Hoenikker number vs. turbulent Langmuir number for experiments with (gray dots) and without (black dots) LSGF from July 13 10:00 UTC to 15:00 UTC. (d) Wave spectrum on July 13 at 14:17 UTC. The dashed and solid circles (inner to outer) correspond to wavelengths of 150, 100, 70, 50, and 30 m. The color scales represent spectral density, linearly spaced from 5% to 95% of the peak spectral density at 5% interval. The red arrow shows the wind vector. The peak spectra density, significant wave height, and dominant wavelength are shown in the lower right corner of the plot. (For interpretation of the references to colour in this figure legend, the reader is referred to the web version of this article.)

$\pi = p/\rho_0 + \frac{1}{2}[|\vec{u} + \vec{u}_s|^2 - |\vec{u}|^2]$ is a generalized pressure. The details on the subgrid scale model, which is only schematically indicated as SGS here can be found in Sullivan et al. (2007), who has introduced the Stokes production into the SGS model. The conservative wave-induced additional diffusivity (e.g., McWilliams et al., 2004; Uchiyama et al., 2010) is insignificant compared with other diffusivity sources and thus ignored in our model. The dynamical equations are integrated in time using third-order Runge–Kutta methods. Horizontal derivatives are evaluated with Fourier pseudo-spectral method. Vertical derivatives are approximated with a high-resolution scheme with flux limiter to suppress spurious oscillation. (e.g., Sullivan et al., 1996 and Sullivan and Patton, 2011). The model has been shown to accurately reproduce observed upper ocean responses to a variety of meteorological conditions without the influence of lateral density gradient (e.g., Kukulka et al., 2009; Liang et al., 2017).

The model domain is set to be rectangular in three dimensions. Periodic boundary conditions are specified for the horizontal directions, outward wave radiation and zero stress are set for the bottom, and no-normal flow and specified momentum and heat fluxes are applied at the surface. Obviously, these treatments of boundary conditions have serious limitations in predicting turbulence in inhomogeneous flow fields, especially those locations that are strongly influenced by larger-scale ocean dynamical features, such as density fronts. River runoff or massive ice melt can create very strong salinity gradients; large temperature and salinity gradients are commonly seen across fronts and eddies which are abundant in the ocean. These submesoscale features can have significant impact on the dynamics and structure of the oceanic mixed layer. It has been also established that small scale turbulence is also important in the dynamics and mixing of the upper ocean and LC is one of the leading causes of turbulent mixing in the upper ocean. Although considerable research has been conducted for both processes separately, our understanding of the interactions between them remains very limited due to the large spatial and temporal scale differences between these two processes. Hamlington et al., (2014) simulated the spin down of a temperature front using a LES model and investigated the effect of LC on submesoscale processes. The effect of submesoscale features on Langmuir turbulence remains unclear.

To study effects of large-scale temperature and salinity fluxes on LC, large-scale gradient forcing (LSGF) is introduced following Wang et al.,

(1998). Computational constraints preclude the possibility of a 2-way coupling of the LES model with a general ocean circulation model. Therefore, a one-way interaction approach is adopted. The underlying assumption is the scale separation hypothesis. It states that the horizontal scales of the large-scale temperature and salinity fluxes are much larger than the scales of motions that are contained within the domain of the LES model, such that the horizontal derivatives of the large-scale terms are unaffected by small-scale motions. By doing so, we can account for the large scale influence on the small scale turbulence while still keeping the periodic boundary condition. The advantage for this approach is that there is no need to impose vertical profiles of velocities, temperature and salinity as horizontal boundary conditions, which may cause wave reflections at the lateral boundaries and interfere with small-scale turbulent motions inside the model domain.

The modified temperature and salinity equations with large scale gradient forcing are given as

$$\frac{D\theta}{Dt} + \vec{u}_s \cdot \nabla\theta = \mathrm{SGS} + \frac{1}{C_p}\frac{\partial I}{\partial z} + H_\theta \tag{2}$$

$$\frac{DS}{Dt} + \vec{u}_s \cdot \nabla S = \mathrm{SGS} + H_s \tag{3}$$

where θ is temperature, S is salinity, $C_p = 4.1 \times 10^6\ \mathrm{J\ m^{-3}\ K^{-1}}$ is the specific heat of seawater per unit volume, and I is the net surface heat flux. The surface freshwater flux term is omitted because there is no precipitation during the study period and the surface evaporation is negligible. H_T and H_S are the large-scale interaction terms for temperature and salinity:

$$H_\theta = -u\frac{\partial \bar{\theta}^L}{\partial \bar{x}^L} - v\frac{\partial \bar{\theta}^L}{\partial \bar{y}^L} \tag{4}$$

$$H_S = -u\frac{\partial \bar{S}^L}{\partial \bar{x}^L} - v\frac{\partial \bar{S}^L}{\partial \bar{y}^L} \tag{5}$$

with the overbar and superscription L (i.e. $\bar{\theta}^L$) stands for large-scale motions. Effects of mesoscale eddy forcing of temperature and salinity are very weak in the study area as indicated by sea surface height anomalies shown in Fig. 1; and hence not considered in this study.

2.3. Model setup

We focus our analysis on data collected at station S5. Temperature and salinity profile time series at this station show deepening of the fresher and warmer upper layer with time with a temperature increase from 27 °C to 30 °C and a salinity decrease from 34 psu to 32 psu at ~20 m between July 7 and July 13 (Fig. 2). Near-surface temperature observations indicate a daily cycle of temperature; however, temperature variations in the upper 10 m are relatively small when compared to its variability below 10 m depth; hence Fig. 2 displays only temperature variations below 10 m. To capture this process, we calculate the large-scale temperature and salinity gradient (H_θ and H_s) using the observed temperature and salinity time series at the four corners of the box (S1 to S4). Since the measurements at S4 started right before July 9, we start our simulation from July 9 at 00:00 UTC and run the model for 5 days to the end of July 13 at 23:00 UTC.

The LES model is configured on a domain of 500 m x 500 m in the horizontal and 70 m in vertical directions. There were 250 grid points in both horizontal directions with a uniform spacing of 2 m. The vertical grid was stretched with a smallest spacing of 0.15 m near the surface to better resolve the boundary layer turbulence (McWilliams et al., 2014).

All model simulations start from rest. Wirewalker measurements of temperature and salinity from July 8 23:45 UTC to July 9 00:15 UTC were averaged in time to create the initial condition for the LES model on July 9 at 00:00 UTC (blue dash line in Fig. 5a and b). Stokes drift profile time series were computed from the wave spectra data, $E(\sigma, \theta)$, collected by the 1200 kHz ADCP at S5 according to Kenyon, (1969):

$$\vec{u}_s = 2\iint \sigma\vec{k}E(\sigma,\theta)e^{-2kz}d\sigma d\theta \tag{6}$$

where σ, θ, and $\vec{k}$ are the frequency, direction, and wave number vector of the spectra. Since the wave spectra are measured in frequency bands range from 0.0083 to 0.9927 Hz, the contribution to Stokes drift from the higher frequencies are omitted. Numerical experiments conducted using SWAN (not shown) have shown that the effect of high frequency tails on Stokes drift profile is significant at the surface (z = 0), especially for low wind speeds, but this effect becomes small around 0.15 m depth (our first model layer) and diminishes around 0.3 m depth for 6 m/s wind or higher. Furthermore, Kukulka and Harcourt (2017) found that "Only waves with wavelengths greater than about 20% of the OSBL depth contribute substantially to deep LT for typical ocean wave ages and wind speeds between 5 and 20 $\mathrm{ms^{-1}}$." Thus, it is safe to assume that our model results are not affect by neglecting the contributions of high frequency tails to the Stokes drift calculations.

Model surface forcing includes wind stress and heat fluxes. Time-varying wind stress, latent, and sensible heat fluxes were calculated based on field measurements using the vectorized COARE 3.0a algorithm modified from Fairall et al., (2003) by Woods Hole Oceanographic Institution (WHOI). Our measurement site resembles typical open ocean wave conditions, thus the option with surface gravity wave effect is not required (Fairall et al., 2003) and thus turned off in the algorithm. Since the instrument measuring long / short wave radiation was not recording data until the very end of the field experiment, the assimilated Coupled Ocean/Atmosphere Mesoscale Prediction System (COAMPS) run at 1 km resolution was used to produce these heat fluxes at S5. All forcing (wind stress, latent and sensible heat fluxes, long / short wave radiation, H_θ and H_s) are given at hourly intervals.

Four LES experiments are conducted: experiment 1 includes no effect from either the LSGF (H_θ and H_s) or Stokes drift velocities, experiment 2 includes the effect of LSGF only, experiment 3 includes the effect of Stokes drift only, and experiment 4 includes both effects.

3. Results

3.1. Water properties and langmuir circulation

The salinity vertical profiles in the four experiments are presented in Fig. 4 from July 11 00:00 UTC to the end of the model simulation on July 13 at 23:00 UTC. The mixed layer depth (h_M) given by white solid/dashed lines for the model/observations is defined as the depth where changes of the potential density are (referenced to surface) less than 0.125 $\mathrm{kg/m^3}$. It is apparent that the water column is much saltier in the top 10–15 m when LSGF is not included. With the same LSGF set up, the inclusion of the Stokes drift always deepens the mixed layer, indicating the enhancement of turbulence in the water column by LC. Interestingly, the largest mixed layer depth discrepancy between model and observations is found in experiment 2 when we consider LSGF only (Fig. 4b). The variation of the salinity profiles with time also shows significant differences from the observations given in Fig. 2b, such as the low salinity spike during July 12 that is not observed at the Wirewalker location, and the shallower intrusion of low salinity waters at the end of July 12 and beginning of July 13. These discrepancies indicate that only having the correct large scale dynamics without proper small scale turbulent mixing may lead to even a worse representation of the water columns.

The salinity variation of the water column in experiment 4 compares best with observations. But due to the coarse resolution of ADCP measurements in both temporal (hourly) and vertical resolution beneath 11 m (every 7 m), the salinity structures are much smoother in the model with shallower penetrations of fresher water. Especially for the two events during July 11 and 12 when the fresher water penetrates to almost 20 m in depth (Fig. 2b), the ADCP measurements and hence

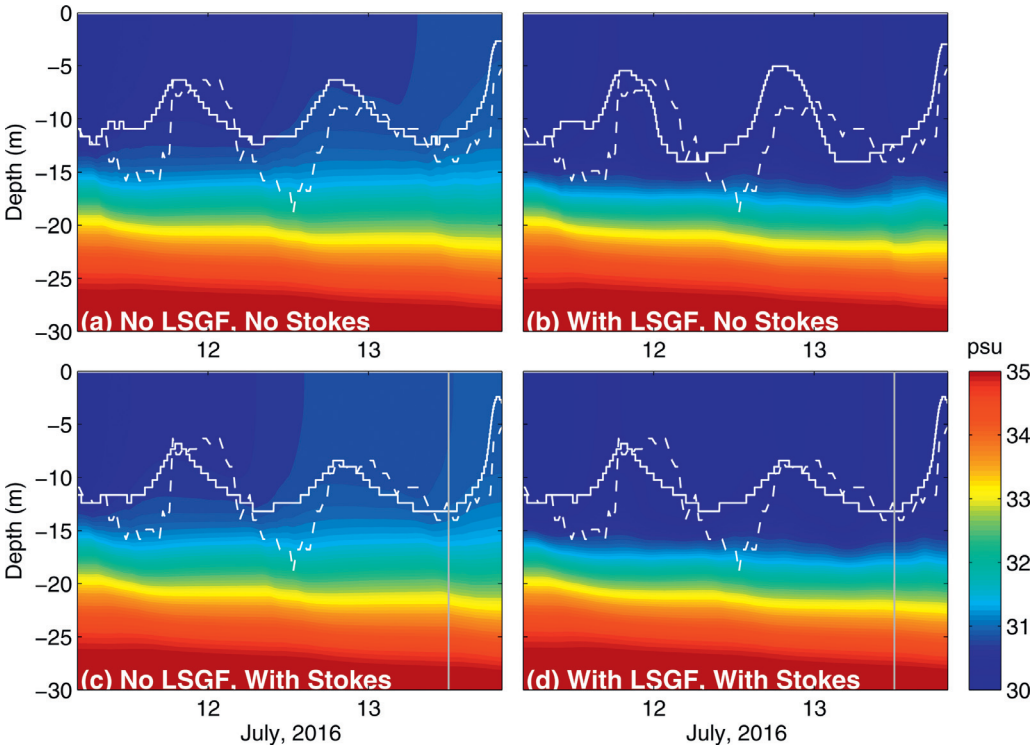

Fig. 4. Model vertical profiles of salinity from July 10 00:00 UTC to July 14 00:00 UTC for LES simulation (a) without LSGF and Stokes drift, (b) With LSGF but without Stokes drift, (c) Without LSGF but with Stokes drift, and (d) with LSGF and Stokes drift. The white dashed and solid lines are mixed layer depth (h_M) calculated using wirewalker measurements and LES model results respectively. The light gray line in (c) and (d) indicates the time for temperature and salinity comparison in Fig. 5.

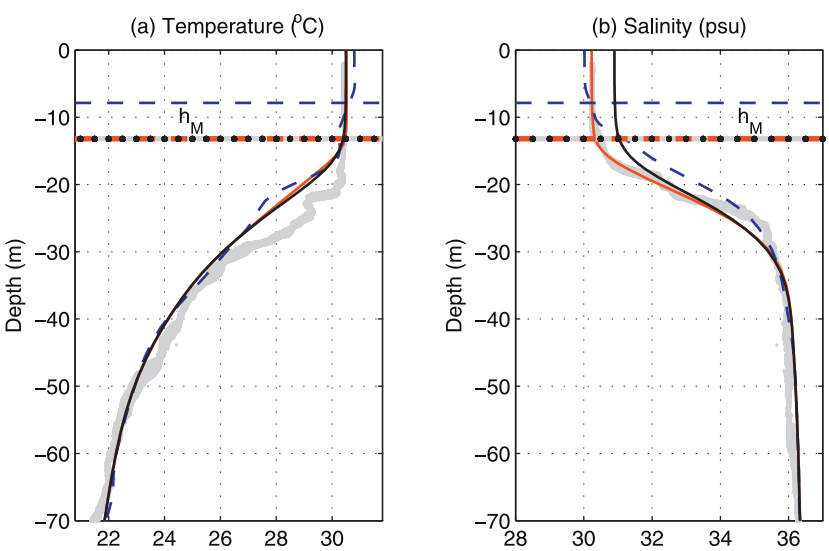

Fig. 5. Vertical profile of (a) temperature and (b) salinity for initial condition (blue dashed line) and model results on July 13 12:00 UTC with (red line) and without (black line) large scale gradient forcing. The gray area indicates Wirewalker observations within 1 h of the model results. The horizontal blue dashed, gray, red dashed, and black dotted lines are h_M calculated using initial conditions, Wirewalker observations, model results with and without large scale gradient forcing, respectively. (For interpretation of the references to colour in this figure legend, the reader is referred to the web version of this article.)

the LSGF only caught part of these penetration resulting in much shallower mixed layer depth in the model.

The vertical profiles of temperature and salinity from the experiments 4 (with LSGF and Stokes drift) and 2 (with Stokes drift but without LSGF) were further compared with the Wirewalker data on July 13 at 12:00 UTC (Fig. 5a, b). When LSGF is included, the modeled salinity profile (red line) matches with observations (gray area) pretty well except for the depths between 20 and 30 m, while the modeled salinity in the experiment without LSGF was overestimated by 0.7 psu in the mixed layer and the overestimation persists for another 10 m or so beneath the mixed layer. On the other hand, the temperature profiles are almost identical between these two experiments. This is because the spatial variation of salinity is mainly in the mixed layer which is sampled with high vertical resolution at the four corners of the box (S1–S4), while the spatial variation of temperature is mainly beneath the mixed layer at ~20 to 40 m in depth where the observations are too sparse to capture the vertical variation of the LSGF. The mismatch of temperature profile beneath the mixed layer also affects the salinity simulation and causes the mismatch between 20 and 30 m.

During this ~5-day simulation period, the turbulent Langmuir number ($La_t = \sqrt{u_*/u_s}$, where u_* is the friction velocity) is around 0.5 (Fig. 3b) indicating combined effects of the wind and wave forcing (Belcher et al., 2012). Since the wind direction oscillates within 30° of the true north most of the time and the wind magnitude varies from 3.8 to 10.6 m/s (Fig. 3a), there are often misalignments between wind and waves, La_t may not be the best representation of the relative importance of Langmuir turbulent to shear instability of the wind driven currents. Van Roekel et al. (2012) have attempted a new approach to capture the importance of Langmuir turbulence under misaligned wind and wave forcing through a projected turbulence Langmuir number, which argues that the orientation of Langmuir circulation should be decided through the tilting of vorticity in the flow field. The concept is attractive, but

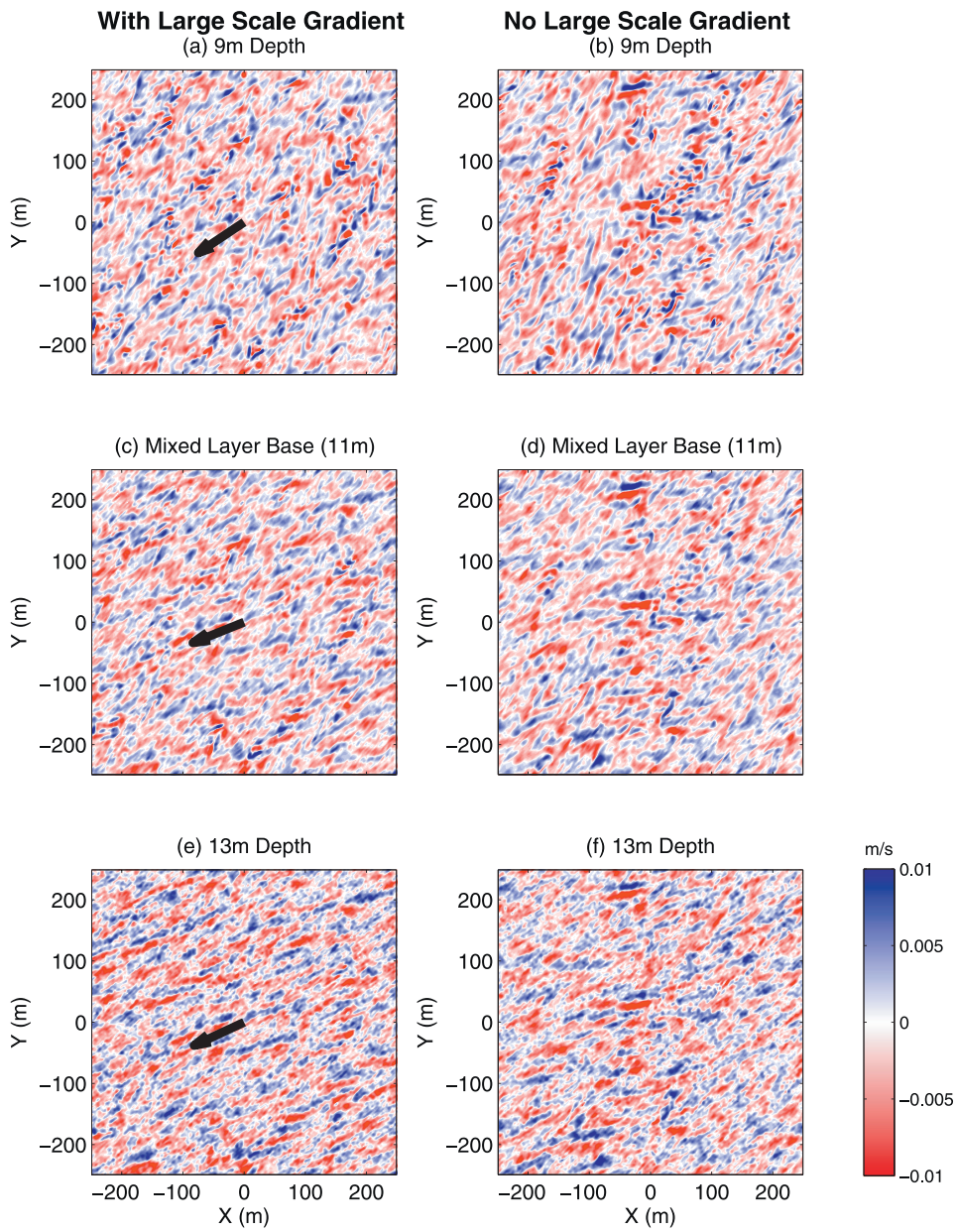

Fig. 6. Snapshots of vertical velocity in m/s at depths of (a) 9 m, (c) 11 m (mixed layer base) and (e) 13 m for the experiment with LSGF. The corresponding plot for the experiment without LSGF are given in (b), (d), and (f). The black arrow gives the large scale pressure gradient direction at the corresponding depth respectively.

their formulation can only be applied to stable results usually found in idealized experiments with constant wind and wave forcing such as Van Roekel et al. (2012), and not practical for real ocean simulations presented in this study.

Towards the end of the simulation, there is a 5 h wind event from 10:00 UTC to 15:00 UTC on July 13, when the wind is roughly unidirectional towards the north with small magnitude variations (red arrows in Fig. 3a). The Hoenikker number H_o ($4B_0/u_s\beta u_*^2$, where B_0 is the surface buoyancy flux, and β is the Stokes drift current e-folding depth) vs. turbulent Langmuir number during this period (Fig. 3c) indicating Langmuir turbulence dominance regime following Li et al. (2005). Snapshots of vertical velocities at the end of this wind event show similar near-surface patterns between the two experiments with organized Langmuir circulation structures of elongated rolls aligned with the wind direction (not shown). The horizontal and vertical scales of the vortices increase with depth and their axis rotates clockwise due to the Ekman spiral effect (McWilliams et al., 1997, 2012). Around the bottom of the mixed layer, the Langmuir rolls rotate to about 50 to 60° relative to the wind direction. They are more organized and align with the large-scale pressure gradient direction in the experiment with LSGF than in the experiment without the background gradient (Fig. 6).

To understand the effect of LSGF on the mean flow and turbulence, we analyze the mean flow, Reynold stress, and turbulence profiles. All statistics in Fig. 8 and 9 are averaged over one inertial period (25.5 h) towards the end of the simulation and normalized by the friction velocity. The boundary layer depth (h_B) is defined using the maximum potential temperature gradient method proposed by Sullivan et al., (1998).

3.2. Mean velocity and momentum balance

The mean flow (averaged over the horizontal domain) fields are dominated by inertial oscillations in both experiments (Fig. 7). The downward propagation of the inertial energy in the model is much weaker compared with the observations for both experiments. This is

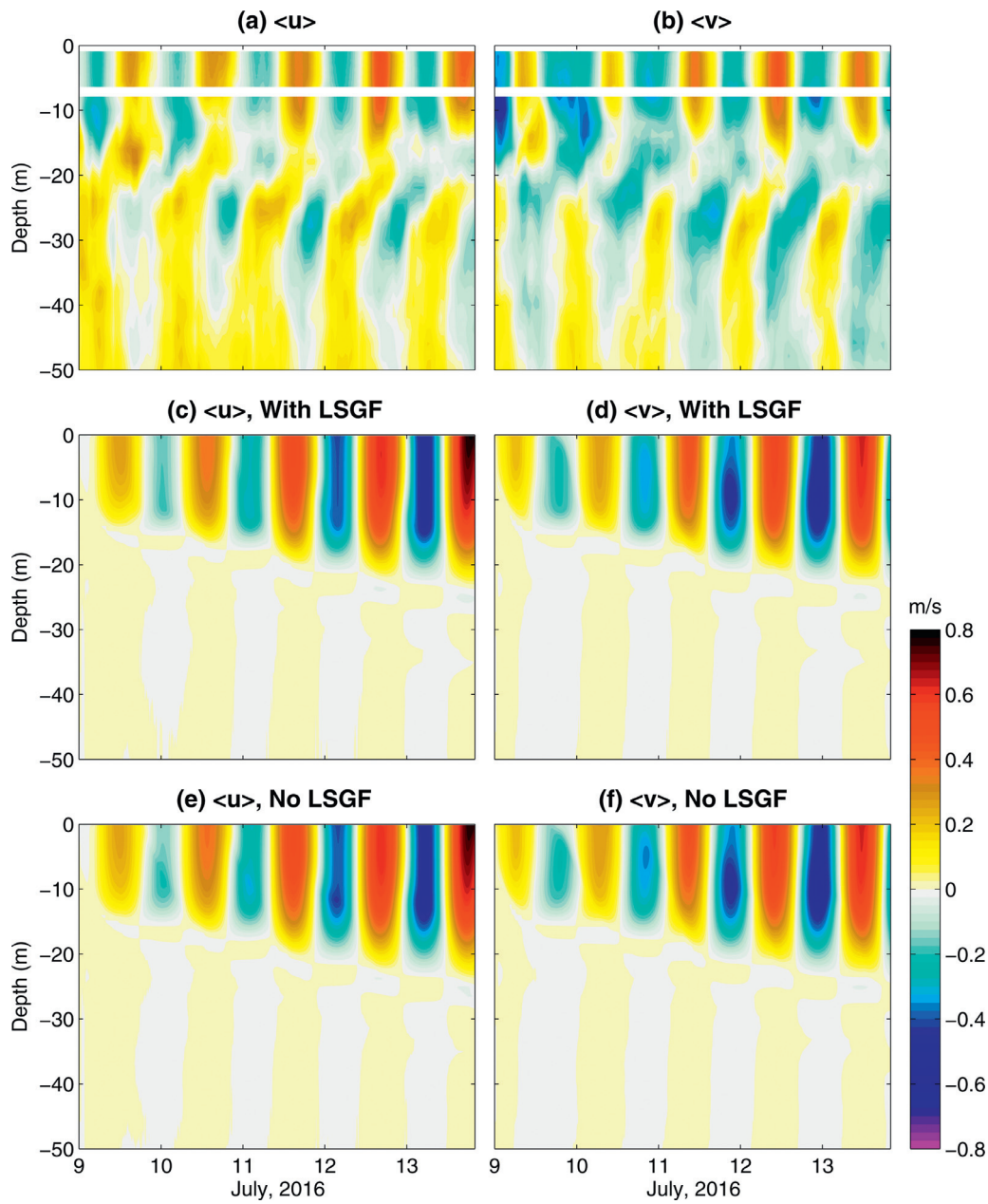

Fig. 7. Observed velocity components (a) u and (b) at station SA5, model velocity components (c) u and (d) v in the case with LSGF, and model velocity components (e) u and (f) v in the case without LSGF.

mainly due to the strong stratification in the study area that inhibits the downward propagation of the inertial energy in the model (Kim et al., 2015) given the short simulation period. Furthermore, the large discrepancies between the modeled and observed temperature and salinity profiles right beneath the mixed layer (Fig. 5) alters the stratification in the model significantly, which may further interfere with the downward propagation of the inertial energy. Due to the reduced downward propagation of the inertial energy, wind inputted energy is trapped in the surface layer and significantly enhances the mean flow in the model.

The mean horizontal velocity ($< u >$, $< v >$) profiles are very similar between these two cases for the ⟨v⟩ component, while the ⟨u⟩ component shows differences from the mid mixed layer to several meters below the boundary layer (Fig. 8a, b). For the LSGF case, the ⟨u⟩ component is slightly larger than that in the case without LSGF within the mixed layer and switched to smaller beneath the mixed layer resulting in the mean surface current direction above/below the mixed layer to be slightly shifted in the clockwise/counterclockwise direction relative to the case without LSGF. This is because the horizontal pressure gradient due to the background salinity variations is strong and dominated by the westward component between the base of the mixed layer and the boundary layer (Fig. 6c and e) and thus causing the eastward component of the velocity to decrease. Although its effect on the magnitude of the mean flow is relatively small, the LSGF seems to be able to rotate the axis of the Langmuir cell rolls and align it with the pressure gradient direction.

The Reynolds stress (Fig. 8c, d) is dominated by the southward component ($< v'w' >$) that is very similar for both experiments, while the westward component ($< u'w' >$) is smaller in the experiment with LSGF from the middle of the mixed layer to several meters beneath the boundary layer because they are strongly constrained by the imposed surface stress and the mean velocity profiles.

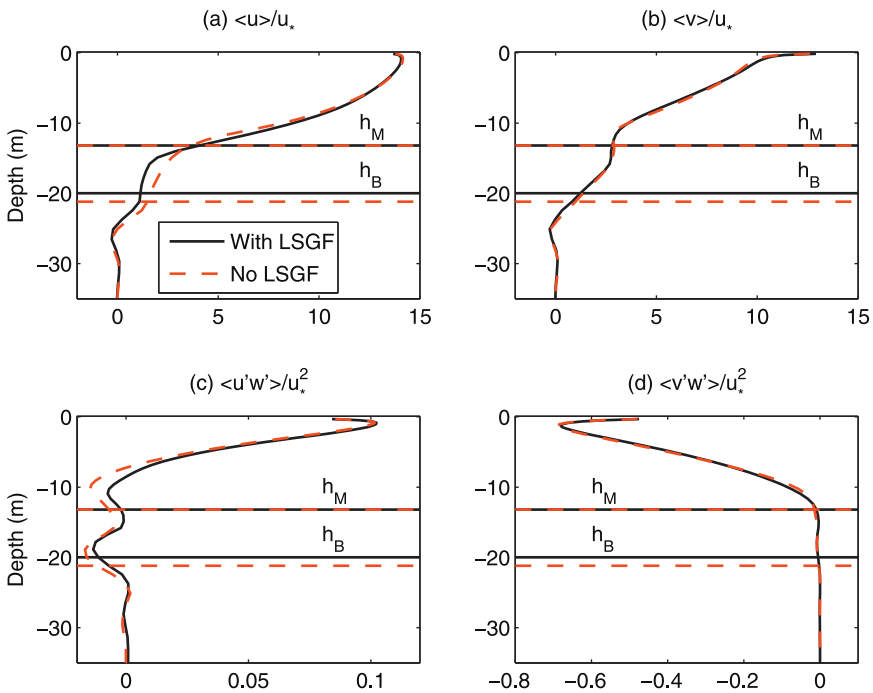

Fig. 8. Mean horizontal velocity profiles: (a) u and (b) v normalized by the friction velocity u_*. Mean turbulent vertical Reynolds stress normalized by u_*^2 in (c) east and (d) north directions. In all panels, the black and red dashed lines represent results from the experiment with and without LSGF, respectively, and h_M and h_B represent the depths of the mixed layer and boundary layer.

3.3. Turbulence

Both the u' and v' variance are smaller with the presence of the LSGF (Fig. 9a, b) with much larger difference in the v' component from the surface all the way to the base of the boundary layer, while there is no difference in the w' variance between these two cases (not shown). As a result, the total TKE that contains both large-eddy and subgrid-scale components are significantly reduced when LSGF is included in the experiment (Fig. 9c).

The turbulent vertical temperature flux $w'\theta'$ (Fig. 9d) appear to have its maximum value at the base of the mixed layer in the experiment with LSGF and then sharply declines with depth; while in the experiment without LSGF, the maximum of $w'\theta'$ is relatively smaller and its variation with depth is smoother with small changes from the bottom of the mixed layer to the base of the boundary layer. The turbulent vertical flux of salinity $w'\theta'$ (Fig. 9e) is smaller in the experiment with LSGF throughout the water column. The largest differences are found in the top 15 m or so where the LSGF significantly alters the salinity structure in the water column with the added fresher water inflow into the model domain (Fig. 4d).

The horizontal averaged budget equation for the resolved turbulent kinetic energy (TKE), e(z), is given as

$$\frac{\partial e}{\partial t} = T + S + B + P + St - \varepsilon \tag{7}$$

where,

$T = -\frac{1}{2}\left(\frac{\partial\langle u'^2w'\rangle}{\partial z} + \frac{\partial\langle v'^2w'\rangle}{\partial z} + \frac{\partial\langle w'^2w'\rangle}{\partial z}\right)$ is the turbulent transport term,

$S = -\langle u'w'\rangle\cdot\frac{\partial\langle u\rangle}{\partial z} - \langle v'w'\rangle\cdot\frac{\partial\langle v\rangle}{\partial z}$ is the shear production term,

$B = \alpha g\langle\theta'w'\rangle - \beta g\langle s'w'\rangle$ is the buoyancy production term,

$P = -\frac{1}{\rho_0}\frac{\partial\langle p'w\rangle}{\partial z}$ is the pressure transport term,

$St = -\langle u'w'\rangle\frac{\partial u_{sx}}{\partial z} - \langle v'w'\rangle\frac{\partial u_{sy}}{\partial z}$ is the Stokes production term,

and ε is the kinetic energy dissipation rate. The angle bracket in the above equations represents horizontal average, the superscript prime denotes a departure from horizontal average. The SGS TKE equation takes the same form as Eq. (7) except the fluxes are parameterized instead of being resolved. For example, the Stokes production in the subgrid model is given as $-\tau_{x_{sub}}\frac{\partial u_{sx}}{\partial z} - \tau_{y_{sub}}\frac{\partial u_{sy}}{\partial z}$ (Sullivan et al., 2007), where the stress ($\tau_{x_{sub}}$, $\tau_{y_{sub}}$) is calculated using parameterized viscosity and current shear. In this study, we will focus on the resolved TKE only.

The TKE balance for the experiment without LSGF is represented by dash lines in Fig. 10a. The shear and Stokes productions are the primary energy sources through the entire boundary layer. The turbulent transport is much weaker and acts to spread energy downward from the more energetic upper part to the lower part of the boundary layer. Its crossover depth from negative to positive is around 2 m, which is ~10% of the boundary layer depth. Interestingly, the pressure transport is also large in the top 2 to 3 m and transports a large amount of TKE down the water column. It is a major contributor to the source terms close to the surface, and quickly crosses over from positive to negative at ~0.5 m and becomes one of the dominant energy sinks between 0.5 m and 2 m.

When LSGF is added to the system, the main difference in the TKE budget are found in the buoyancy production and the pressure transport in the boundary layer and below 2 m depth. Thus, these two terms are zoomed in and compared for depths between 2 and 22 m in Fig. 10b. When LSGF is included, the buoyancy production is smaller and its crossover depth from positive to negative values is shallower indicating stabilizing effects in the boundary layer and thus inhibits turbulence. In other words, the fresh water inflow causes energy consumption through an increase in the potential energy of the water column through mixing. Correspondingly, the crossover depth for the pressure transport from negative to positive is deeper with the LSGF included, which means more energy is transported downward. The joint effect of the lower buoyancy production and more negative pressure transport decreases the total TKE and reduces the turbulence level in the water column. Changes in the buoyancy production and pressure transport also cause a redistribution of energy in the shear production, turbulent transport, and dissipation, but interestingly, the Stokes production barely changes, i.e., the difference between the two experiments is so small that it is not identified visually.

4. Discussions and conclusion

Langmuir circulation (LC) is believed to be one of the leading causes of turbulent mixing in the upper ocean. LES models have been used to

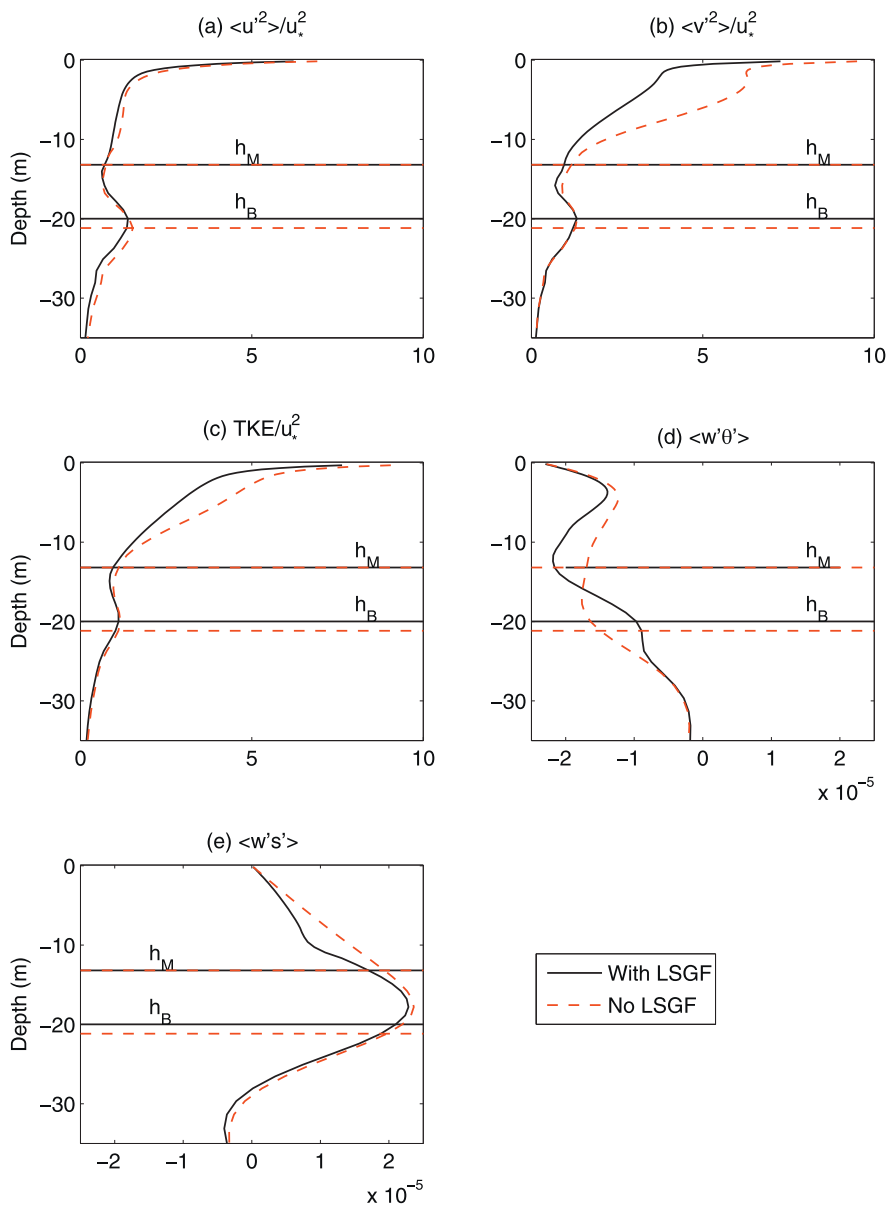

Fig. 9. Profiles of large eddy fluctuation velocity component variances (a) u'^2 and (b) v'^2 normalized by u_*^2, (c) total TKE normalized by u_*^2, and the vertical turbulent flux of (d) temperature in K m s^{-1}, and (e) salinity in psu m s^{-1}. The black and red dashed lines represent results from the experiment with and without LSGF, respectively. h_M and h_B in all panels represent the mixed layer and boundary layer depth. (For interpretation of the references to colour in this figure legend, the reader is referred to the web version of this article.)

study LC in the upper ocean for the past two decades. Due to its high computational cost, the LES studies are usually limited to a finite domain with hundreds of meters at each horizontal direction and are not able to resolve large-scale flows. Most of these LES models for LC simulations use periodic boundary conditions in the horizontal directions that can significantly reduce computational effort. However, such treatment of boundary conditions has serious limitations in predicting turbulence in inhomogeneous flow fields, especially in those locations that are strongly influenced by larger-scale oceanic dynamical features such as fronts that can have significant impact on the dynamics and structure of the oceanic mixed layer (D' Asaro et al., 2011).

The present study expands the previous LES modeling investigations of Langmuir turbulence to real ocean conditions with large-scale environmental motion due to the strong horizontal density gradient, which are commonly seen along oceanic fronts, eddies, and river discharge areas. Large scale gradient forcing (LSGF) is introduced to the NCAR LES model through the scale separation analysis. The model is applied to field observations from the Gulf of Mexico collected in July 2016 when the measurement site was impacted by the large fresh water inflow due to flooding from the Mississippi/Atchafalaya River System.

Model results agree with previous studies that LC enhances turbulence in the water column and deepens the mixed layer with or without LSGF. The large horizontal density gradient can reduce the mean flow in the ML. It also helps to organize the Langmuir cells and align the roll axis along the pressure gradient direction. Because the fresh water inflow causes energy consumption through an increase in the potential energy of the water column through mixing, the buoyancy production is smaller and its crossover depth from positive to negative values is shallower and thus helps to stabilize the water column. Correspondingly, more energy is transported downward through the pressure transport, and the total TKE is reduced and hence the turbulence level is also diminished in the water column. Changes in the buoyancy production and the pressure transport also cause a redistribution of the energy in the shear production, turbulent transport, and

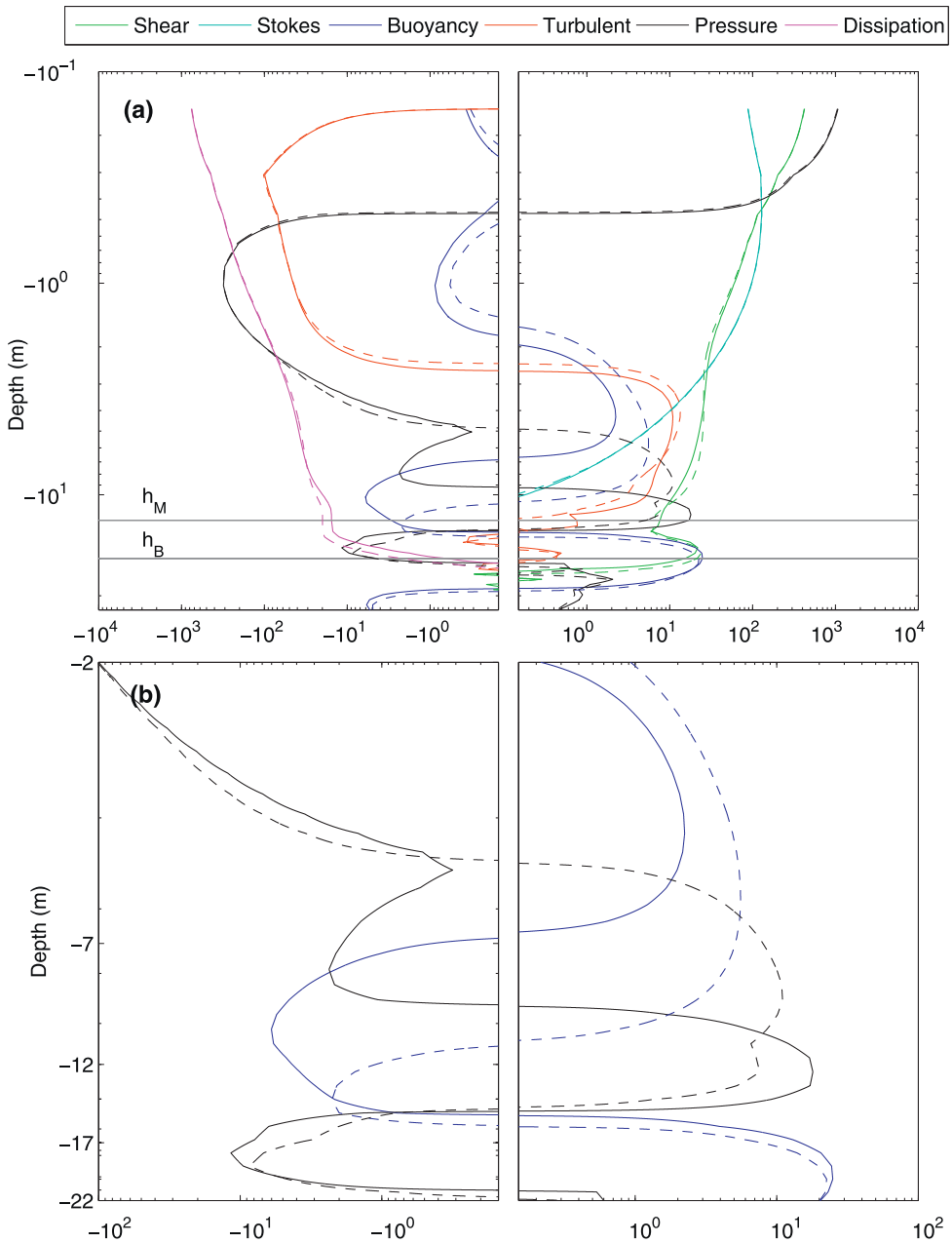

Fig. 10. (a) TKE balances in m^2s^{-3} for the experiment with LSGF (solid) and without LSGF (dashed) on a split log-log scale. Individual terms for shear production, Stokes production, buoyancy production, turbulent transport, pressure transport, and dissipation are given in the legend. (b) Zoomed in figure of the variation of buoyance production and pressure transport between 2 m and 22 m depth only.

dissipation, while the Stokes production remains unchanged.

We think that this stabilizing effect should be present whenever a strong horizontal density gradient is present, but how important this effect is depends on the dynamics of the individual situation that is examined. This study is limited in many ways, such as the inadequate representation of the LSGF due to the coarse temporal and vertical resolution of the temperature and salinity measurements. Especially the inability of the proper approximation of the large scale temperature fluctuations beneath the mixed layer significantly alters the stratification in the model compared with observations and thus limits our understanding of the mechanisms that may impact the stabilizing effect. More studies are required to further understand these effects. For example, current study is conducted within a marginal Langmuir regime with weak Stokes drift, so the turbulent enhancement from the surface waves are relatively weak. For strong Langmuir dominated regimes, we would expect the stabilizing effect to be less important.

While small scale turbulence is very important in the dynamics and mixing of the upper ocean, submesoscale features can also have significant impact on the dynamics and structure of the oceanic mixed layer. Although considerable research has been conducted for both processes separately, our understanding on the interactions between them remains very limited due to the large spatial and temporal scale differences between these two processes. Our study has emphasized the importance of large scale motions on small scale turbulence which is usually assumed to be isotropic, while Hamlington et al. (2014) simulated the spin down of a temperature front using a LES model and investigated the effect of LC on submesoscale processes. More studies are required to study the two-way interactions between these two processes. Multiscale numerical algorithm proposed by Malecha et al. (2013) to simulate Langmuir circulation dynamics at submesoscales could be a good approach for this purpose.

Acknowledgment

The authors thank Dr. Peter Sullivan for providing the LES model for this study. This work was funded by the Office of Naval Research under program element 0602435N. This paper is contribution NRL/JA/7320-17-3638 and has been approved for public release. We would like to express our appreciation to the anonymous reviewers for their constructive comments. Observations presented in the manuscript are open-access data. Contact Dr. Ewa Jarosz for accessing the data.

References

Belcher, S.E., and co-authors, 2012. A global perspective on Langmuir turbulence in the ocean surface boundary layer. Geophys. Res. Lett. 39https://doi.org/10.1029/2012GL052932. L18605.

Chini, G.P., Leibovich, S., 2005. Resonant Langmuir-circulation internal-wave interaction. Part 2. Langmuir circulation instability. J. Fluid Mech. 524, 99–120.

Craik, A.D.D., Leibovich, S., 1976. A rational model for Langmuir circulations. J. FluidMech. 73, 401–426. https://doi.org/10.1017/S0022112076001420.

D'Asaro, E., Lee, C., Rainville, L., Harcourt, R., & Thomas, L. (2011). Enhanced turbulence and energy dissipation at ocean fronts.

Fairall, C.W., Bradley, E.F., Hare, J.E., Grachev, A.A., Edson, J.B., 2003. Bulk parameterization of air sea fluxes: updates and verification for the COARE algorithm. J. Climate 16, 571–590.

Hamlington, P.E., Van Roekel, L.P., Fox-kemper, B., Julien, K., Chini, G.P., 2014. Langmuir–Submesoscale Interactions: descriptive analysis of multiscale frontal spindown simulations. J. Phys. Oceanogr. 44, 2249–2272. https://doi.org/10.1175/JPO-D-13-0139.1.

Kenyon, K.E., 1969. Stokes drift for random gravity waves. J. Geophys. Res. 74 (28), 6991–6994.

Kim, S.Y., Kurapov, A.L., Kosro, P.M., 2015. Influence of varying upper ocean stratification on coastal near-inertial currents. J. Geophys. Res. Oceans 120, 8504–8527. https://doi.org/10.1002/2015JC011153.

Kukulka, T., Plueddemann, A.J., Trowbridge, J.H., Sullivan, P.P., 2009. Significance of Langmuir circulation in upper ocean mixing: comparison of observations and simulations. Geophys. Res. Lett. 36. L10603. doi:10.1029/2009GL037620.

Kukulka, T., Plueddemann, A.J., Trowbridge, J.H., Sullivan, P.P., 2010. Rapid mixed layer deepening by the combination of Langmuir and Shear instabilities: a case study. J. Phys. Oceanogr. 40, 2381–2400. https://doi.org/10.1175/2010JPO4403.1.

Kukulka, T., Plueddemann, A.J., Trowbridge, J.H., Sullivan, P.P., 2011. The influence of crosswind tidal currents on Langmuir circulation in a shallow ocean. J. Geophy. Res. 116. C08005. doi:10.1029/2011JC00697.

Kukulka, T., Harcourt, R.R., 2017. Influence of Stokes Drift Decay Scale on Langmuir Turbulence. J. Physic. Oceanogr. 1637–1656.

Li, M., Zahariev, K., Garrett, C., 1995. Role of Langmuir Circulation in the Deepening of the Ocean Surface Mixed Layer. Science 270, 1955–1957.

Li, M., Garrett, C., Skyllingstad, E., 2005. A regime diagram for classifying turbulent large eddies in the upper ocean. Deep Sea Res. Part I 52 (2), 259–278.

Liang, J.-H., Emerson, S.R., D'Asaro, E.A., McNeil, C.L., Harcourt, R.R., Sullivan, P.P., Yang, B., Cronin, M.F., 2017. On the role of sea-state in bubble-mediated air-sea gas flux during a winter storm. J. Geophys. Res. 122, 2671–2685.

Malecha, Z., Chini, G.P., Julien, K., 2013. A multiscale algorithm for simulating spatially-extended Langmuir circulation dynamics. J. Comput. Phys. 271, 131–150. https://doi.org/10.1016/j.jcp.2013.07.003.

Martinat, G., Xu, Y., Grosch, C.E., Tejada-Martínez, A.E., 2011. LES of turbulent shear flow and pressure gradient driven flow on shallow continental shelves. Ocean Dyn. 9, 1369–1390.

McWilliams, J.C., Sullivan, P.P., Hoeng, C., 1997. Langmuir turbulence in the Ocean. J. Fluid Mech. 334, 1–30.

McWilliams, J.C., Restrepo, J.M., Lane, E.M., 2004. An asymptotic theory for the interaction of waves and currents in coastal waters. J. Fluid Mech. 511, 135–178.

McWilliams, J.C., Huckle, E., Liang, J., Sullivan, P.P., 2014. Langmuir turbulence in swell. J. Phys. Oceanogr. 44, 870–890. https://doi.org/10.1175/JPO-D-13-0122.1.

Pinkel, R., Goldin, M.A., Smith, J.A., Sun, O.M., Aja, A.A, Bui, M.N., Hughen, T., 2011. The Wirewalker: a vertically profiling instrument carrier powered by ocean waves. J. Atmos. Oceanic Technol. 28, 426–435.

Polton, J.A., Smith, J.A., MacKinnon, J.A., Tejada-Martínez, A.E., 2008. Rapid generation of high-frequency internal waves beneath a wind and wave forced oceanic surface mixed-layer. Geophys. Res. Lett. 35 L13602.

Skylingstad, E.D., Denbo, D.W., 1995. An ocean large-eddy simulation of Langmuir circulations and convection in the surface mixed layer. J. Geophys. Res 100 (5), 8501–8522.

Sullivan, P.P., McWilliams, J.C., Moeng, C.-H., 1996. A grid nesting method for large-eddy simulation of planetary boundary layer flows. Boundary-Layer Meteorol. 80, 167–202.

Sullivan, P.P., Moeng, C.-H., Stevens, B., Lenschow, D.H., Mayor, S.D., 1998. Structure of the entrainment zone capping the convective atmospheric boundary layer. J. Atmos. Sci. 55, 3042–3064.

Sullivan, P.P., McWilliams, J.C., Melville, W.K., 2007. Surface gravity wave effects in the oceanic boundary layer: large-eddy simulation with vortex force and stochastic breakers. J. Fluid Mech. 593, 405–452. https://doi.org/10.1017/S002211200700897X.

Sullivan, P.P., Patton, E.G., 2011. The effect of mesh resolution on convective boundary layer statistics and structures generated by large-eddy simulation. J. Atmos. Sci. 68, 2395–2415.

Suzuki, N., Fox-Kemper, B., 2016. Understanding Stokes forces in the wave-averaged equations. J. Geophys. Res. Oceans 121, 3579–3596. https://doi.org/10.1002/2015JC011566.

Terray, E.A., Brumley, B.H., Strong, B., 1999. Measuring waves and currents with an upward looking ADCP. In: Proc. IEEE 6th Working Conference on Current Measurement. IEEE, New York, pp. 66–71.

Uchiyama, Y, McWilliams, J.C., Shchepetkin, A.F., 2010. Wave–current interaction in an oceanic circulation model with a vortex-force formalism: application to the surf zone. Ocean Modell. https://doi.org/10.1016/j.ocemod.2010.04.002.

Van Roekel, L.P., Fox-Kemper, B., Sullivan, P.P., Hamlington, P.E., Haney, S.R., 2012. The form and orientation of Langmuir cells for misaligned winds and waves. J. Geophys. Res. Oceans 117 (C5). https://doi.org/10.1029/2011JC007516.

Wang, D., McWilliams, J.C., Large, W.G., 1998. Large-eddy simulation of the diurnal cycle of deep equatorial turbulence. J. Phys. Oceanogr. 28, 129–148.